energy&fuels

Article

pubs.acs.org/EF

# Mn-Catalyzed Oxidation of Heavy Oil in Porous Media: Kinetics and Some Aspects of the Mechanism

Andrey Galukhin,*[,†,‡] Mohammed Amine Khelkhal,[†,‡] Alexander Gerasimov,[†] Timur Biktagirov,[‡,§] Marat Gafurov,[§] Alexander Rodionov,[§] and Sergei Orlinskii[§]

[†]Institute of Chemistry, [‡]Institute of Geology and Petroleum Technologies, and [§]Institute of Physics, Kazan Federal University, 18 Kremlevskaya Street, Kazan 420008, Russian Federation

Supporting Information

**ABSTRACT:** Mn-catalyzed oxidation of the Ashalcha heavy oil in porous media was examined. We used manganese(III) tris(acetylacetonate) as a convinient oil-soluble precatalyst that decomposes to catalytically active species during the temperature ramping. Reaction kinetics in the heavy oil oxidation with air indicated that the presence of the manganese ions changes the mechanism of the oxidation process, especially in the high-temperature region. To study precatalyst transformations in detail, we suggested the approach of combining X-ray powder diffraction (XRPD), thermal analysis, non-isothermal kinetic methods, and electron paramagnetic resonance (EPR). A comprehensive study of the decomposition of pure manganese(III) tris(acetylacetonate) and the subsequent comparison of its behavior to that in porous media in the presence of the oil allows us to shed light on some aspects of the mechanism of catalytic oxidation.

## 1. INTRODUCTION

The increasing consumption of energy resources accompanied by the shortage of conventional fossil fuels demands the exploitation of heavy oil reservoirs as one of the most abundant hydrocarbon storages.[1] Petroleum production companies usually apply thermally enhanced oil recovery (TEOR) methods based on steam injection processes to exploit such kinds of oil reservoirs. Steam generation for TEOR consumes natural gas and produces a vast amount of carbon oxides as a byproduct.[2] Moreover, a significant amount of the generated heat is wasted during steam transfer through pipelines to formation. Direct heat generation inside an oil reservoir allows for a significant decrease of heat loses and reduces greenhouse gas emission. One of the most promising approaches applied to the development of heavy oil formations is *in situ* combustion (ISC).[3,4] During ISC, air is injected into a reservoir to oxidize a small portion of the hydrocarbons to generate heat and pressure that enhance recovery. Stability of the smoldering front is considered to be a key parameter determining the success of the ISC process.[5] Catalyst application promotes the oxidation process and significantly improves oil properties.[6] Conversion to high-quality oil has become an important issue as a result of its potential to solve the conventional fossil fuel shortage and environmental problems. Despite a large number of studies related to *in situ* catalytic oil oxidation, there were no attempts of profoundly serious investigation of the role of catalysts in this complex process, and transformations of catalysts still remain to be a "black box".

Manganese-based catalysts attract significant attention as heterogeneous catalysts for both full and partial oxidation of organic matter with molecular oxygen.[7−15] High catalytic activity, diverse oxidation states coupled with low toxicity, and ready availability make Mn-based oxidation catalysts superior compared to other transition metals. This set of properties makes Mn-based catalysts excellent candidates to facilitate smoldering combustion of organic matter.

In the present study, we investigated Ashalcha heavy oil oxidation in porous media in the presence of manganese oxide particles formed *in situ* from an oil-soluble catalyst precursor. We applied conventional thermal analysis methods coupled with electron paramagnetic resonance (EPR) and X-ray powder diffraction (XRPD) methods to study precatalyst transformations during the heavy oil oxidation. The suggested approach helps to shed light on the mechanism of catalytic oxidation of hydrocarbons in porous media.

## 2. EXPERIMENTAL SECTION

**2.1. Materials.** The crude oil used in this research was extracted from oil core taken from the Ashalcha oilfield (Volga-Ural basin, Republic of Tatarstan, Russia).[16,17] The physical properties and elemental and saturate, aromatic, resin, and asphaltene (SARA) analysis data of crude oil are given in Table 1. Organic solvents, such as toluene, heptane, dichloromethane, and methanol (purity of all solvents was no less than 99.5%), were purchased from Component-Reaktiv and used without additional purification. Inorganic salts and aluminum oxide (particle size of 0.05−0.15 mm, neutral) were purchased from Sigma-Aldrich.

*2.1.1. Manganese(III) Tris(acetylacetonate) [Mn(AcAc)$_3$] Preparation.* $Mn(AcAc)_3$ was prepared according to a well-known procedure[18] with additional purification via recrystallization from a heptane−toluene mixture to remove the impurity of manganese(II) bis(acetylacetonate) [$Mn(AcAc)_2$] (see the Supporting Information).

*2.1.2. Sample Preparation for Kinetic Analysis.* Samples for DSC analysis were prepared by mixing the heavy oil (20.0 wt %) and porous matrix ($Al_2O_3$, 80.0 wt %). In the case of catalytic experiments, an initial oil sample contained 2 wt % $Mn(AcAc)_3$. This sample is denoted as Mn−$Al_2O_3$−oil throughout the text.

**Received:** May 23, 2016
**Revised:** August 8, 2016
**Published:** August 9, 2016

  

DOI: 10.1021/acs.energyfuels.6b01234
*Energy Fuels* 2016, 30, 7731−7737

**Table 1. Physical Properties of Ashalcha Heavy Oil at 20 °C**

| | | | elemental content (%) | | | | SARA analysis (%) | | | |
|---|---|---|---|---|---|---|---|---|---|---|
| viscosity (mPa s) | density (g cm$^{-3}$) | API gravity (deg) | C | H | N | S | saturate | aromatic | resin | asphaltene |
| 11811 | 0.97 | 13.8 | 82.09 | 10.12 | 0.63 | 2.65 | 26.2 ± 0.5 | 44.1 ± 0.6 | 26.3 ± 0.5 | 4.5 ± 0.3 |

*2.1.3. Sample Preparation for EPR Analysis of Mn(AcAc)$_3$ Deposited on Aluminum Oxide.* A total of 120 mg of Mn(AcAc)$_3$ was dissolved in 3 mL of anhydrous dichloromethane in a round-bottom flask; then 2.988 g of $Al_2O_3$ was added to the flask; and the obtained final mixture was shacked for 5 min. Then, the solvent was evaporated with a Hei-VAP rotary evaporator (Heidolph) under reduced pressure (20 mbar and 40 °C). This sample is denoted as Mn−$Al_2O_3$. For other investigated EPR samples [Mn(AcAc)$_3$ and Mn−$Al_2O_3$−oil], no special probe preparation was needed.

*2.1.4. Sample Preparation for XRPD Studies of Phase Transformations during Decomposition of Mn(AcAc)$_3$.* Mn(AcAc)$_3$ samples were heated in an electric oven to a certain temperature and then maintained at that temperature for 5 min. XRPD studies were carried out after cooling samples to room temperature.

**2.2. Methods.** *2.2.1. Thermal Analysis.* Thermogravimetric analysis (TGA) and differential scanning calorimetry (DSC) experiments were carried out with thermal analyzer Netzsch STA 449 F3 Jupiter. The experiments were conducted at linear heating rates of 1 °C/min for TGA of Mn(AcAc)$_3$ and 5, 10, 15, and 20 °C/min for kinetic analysis of heavy oil samples, under atmospheric air flow (50 mL/min). The samples were heated from ambient to 600 °C. An average sample was 10 mg for each run. The obtained thermogravimetry (TG) and DSC curves were processed by Proteus analysis (version 5.2.1), NETZSCH peak separation (version 2010.09), and NETZSCH Thermokinetics 3.1 (version 06.08.2014) program packs. For evaluation of kinetic parameters of the oxidation process, non-isothermal kinetic analysis coupled with an isoconversional (model-free) method was used. Two integral isoconversional methods, namely, Kissinger−Akahira−Sunose and Ozawa−Flynn−Wall, were applied to DSC data.[19,20]

*2.2.2. Scanning Electron Microscopy (SEM).* SEM measurements were carried out using a field-emission high-resolution scanning electron microscope Merlin Carl Zeiss. Photo observation of the morphology surface was applied at an accelerating voltage of the incident electron of 15 kV and a current probe of 300 pA to minimally modify samples.

*2.2.3. XRPD.* XRPD studies were made using a MiniFlex 600 diffractometer (Rigaku) equipped with a D/teX Ultra detector. Cu K$\alpha_1$ radiation (40 kV and 15 mA) was used, and data were collected at 25 °C in the range of 2$\theta$ from 2° to 100° with a step of 0.02° and exposure time at each point of 0.24 s without sample rotation.

*2.2.4. EPR.* EPR spectra were recorded by a Bruker ESP-300 spectrometer operating at 9.5 GHz (X band) in continuous wave mode. For temperature ramping in the range of 25−532 °C, the high-temperature resonator ER 4114HT was exploited. During these experiments, the rate of heating was 2 °C/min. In the oil-containing samples, the typical signals of vanadyl porphyrin and organic radical additionally manifest in the spectra[21] but their temperature variations were not the focus of the present study and, thus, were ignored during the analysis.

Quantitative analysis of experimental EPR data was carried out using a home-built MATLAB code. At the first step, this involved a Levenberg−Marquardt nonlinear least squares fit of the experimental spectra by a sum of first-derivative Lorentzian functions. The fit was followed by analytical evaluation of the integral intensity of each spectral component (which corresponds to double integration of the conventionally observed EPR experiment first-derivative curves). For the further analysis of the quantities of interest and the uncertainty of the fit (standard errors and cross-correlations between the fitting parameters), a bootstrap approach based on the residual resample scheme was used.[22] Within the temperature ranges where the described fitting procedure is intractable as a result of the presence of undetermined signals (with no prior information about its line shape), the relative change of the Lorentzian line was estimated by a modified multivariate curve resolution alternating least squares (ALS) method.[23] This was based on the assumption that neither the width of the Loretzian line nor the line shapes of the other components change within the analyzed temperature range. At each subsequent iteration, the algorithm imposed a non-negativity constraint for intensities of independent components and fitted the chosen spectral component by a first-derivative Lorentzian curve.

## 3. RESULTS AND DISCUSSION

TGA of the Mn(AcAc)$_3$ shows that the decomposition under an air atmosphere during temperature ramping proceeds stepwisely (Figure 1). We suggest as a first step (mass change

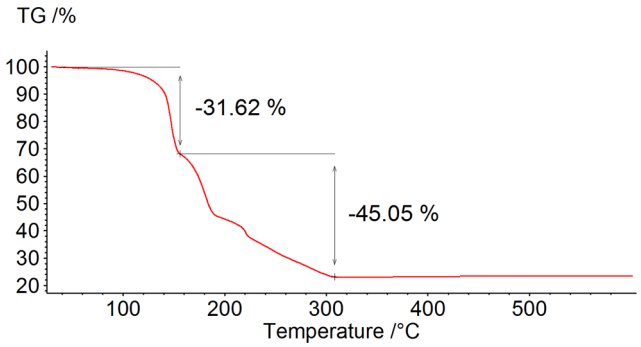


**Figure 1.** TG curve of Mn(AcAc)$_3$ decomposition.

of 31.62%) that Mn(AcAc)$_3$ is reduced into Mn(AcAc)$_2$ with the formation of the acetylacetonate (AcAc) radical (Scheme 1). The formation of radical intermediates during decomposition of organic Mn(III)-containing salts is well-known and used as a key tool of synthetic organic chemistry in the field of free-radical-assisted reactions.[24] Additionaly, this suggestion was proven by XRPD analysis of the samples (Figure 2) and subsequent EPR studies.

**Scheme 1. Suggested Chemical Process Occurring at the First Step of Mn(AcAc)$_3$ Decomposition**

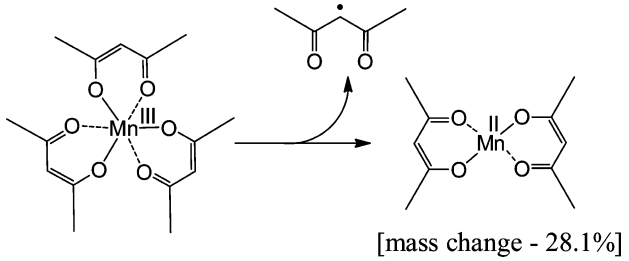


We applied XRPD analysis to investigate phase transformation during Mn(AcAc)$_3$ decomposition (Figure 2). XRPD analysis shows consecutive formation of Mn(AcAc)$_2$, $Mn_3O_4$, and, finally, $Mn_2O_3$ (Scheme 2).

We also used SEM to examine morphology of $Mn_2O_3$ obtained by Mn(AcAc)$_3$ decomposition at an air atmosphere. The result is presented in Figure 3. It could be seen that the decomposition product is presented by sintered $Mn_2O_3$


DOI: 10.1021/acs.energyfuels.6b01234
Energy Fuels 2016, 30, 7731−7737

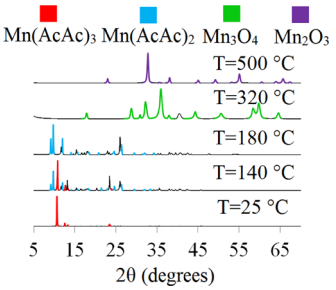


**Figure 2.** XRPD analysis of phase transformations during decomposition of $Mn(AcAc)_3$.

**Scheme 2. Scheme of $Mn(AcAc)_3$ Decomposition According to XRPD Analysis**

$$Mn(AcAc)_3 \longrightarrow Mn(AcAc)_2 \longrightarrow Mn_3O_4 \longrightarrow Mn_2O_3$$

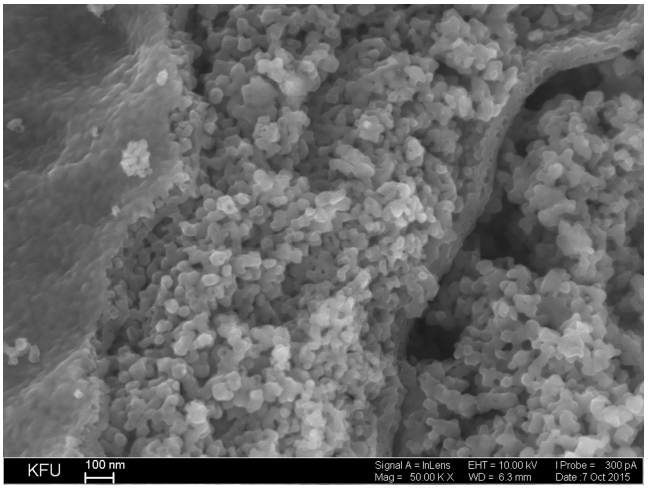


**Figure 3.** SEM image of nanostructured $Mn_2O_3$ formed by decomposition of $Mn(AcAc)_3$.

nanoparticles with a mean size of 44 ± 5 nm (for EDX analysis results, see the Supporting Information).

TGA and XRPD analysis data (Figures 1 and 2) show good agreement with the results obtained by EPR spectroscopy (see below). Different oxidation states of manganese could be detected by EPR, among which Mn(II) with five unpaired 3d electrons and relatively long relaxation times is the most observable and familiar. The registration of other oxidation states is very specific (usually as a result of the large zero-field splitting in crystals) and generally rarely possible in the conventional X-band conditions, especially at elevated temperatures (low temperatures, high frequencies, and special parallel-mode EPR cavities are required).[25] Thus, EPR can shed light on both the chemical environment of manganese in the samples and its charge state. Figure 4 shows the comparison between the $Mn(AcAc)_3$ and $Mn–Al_2O_3$–oil systems subjected to thermal treatment (500 °C). This allowed us to detect a typical six-line hyperfine (HF) pattern with HF splitting of 9.9(1) mT for isolated Mn(II) ions ($S = {}^5/_2$, $I = {}^5/_2$, and $m_S = {}^1/_2 \leftrightarrow m_S = -{}^1/_2$ transition). This signal is superimposed by a broad line (with the peak-to-peak line width of about 35 mT), which can be due to the presence of clusters of manganese ions for which the HF structure is unresolved as a result of the strong spin–spin coupling. Because XRPD data (Figure 2) indicate the presence of crystal phases across the whole temperature range,

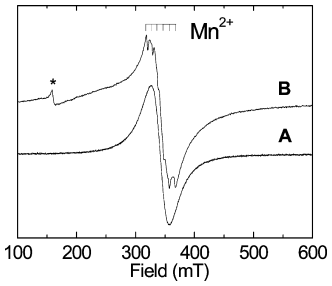


**Figure 4.** Room-temperature X-band EPR spectra of the products of thermal decomposition (532 °C) of (A) pure $Mn(AcAc)_3$ and (B) $Mn–Al_2O_3$–oil systems. The well-resolved HF structure with HF splitting of 9.9(1) mT is due to the presence of Mn(II) ions. The low-intensive signal at 160 mT (marked by an asterisk) is due to impurities in $Al_2O_3$.

the latter signal can be associated with crystalline manganese oxide (e.g., $Mn_3O_4$ crystals were reported to give an EPR line with the line width of 35 mT at room temperature,[26] whereas $Mn_2O_3$ nanocrystals are expected to give a broad asymmetric spectral line of 240–320 mT).[27] When considering $Mn(AcAc)_3$ without $Al_2O_3$, we do not observe the signal corresponding to the weakly coupled Mn(II) (Figure 4). This naturally suggests that, in the absence of an inorganic template, all manganese ions are involved in manganese oxide formation and, consequently, are clusterized. Thus, at the end of the heating course (532 °C), the sample exhibits only a single EPR line of Lorentzian shape (17 mT at 532 °C and 32 mT after cooling to room temperature), which we attribute to the oxide crystal phase (Figure 5).

Notably, we also detected a broad asymmetric signal within a limited temperature range of 266–394 °C (blue line spectra on Figure 5), which partially matched the one on the TG curve,

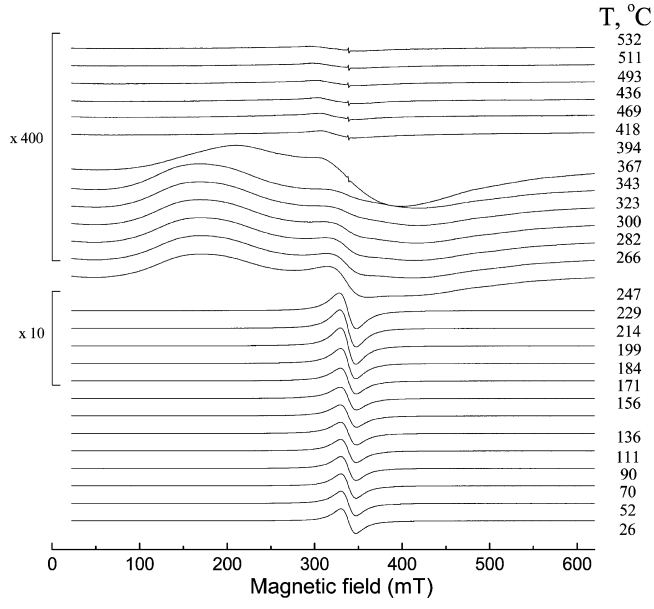


**Figure 5.** Temperature dependence of the EPR spectrum of $Mn(AcAc)_3$ powder under an oxygen atmosphere. The spectra containing the contributions associated with the AcAc radical are shown by blue lines (in the range of 156–247 °C). The spectra in 171–247 and 266–532 °C ranges are detected at the lower gain values compared to the near-room-temperature spectra (in 10 and 400 times, respectively).



DOI: 10.1021/acs.energyfuels.6b01234
Energy Fuels 2016, 30, 7731–7737

where decomposition of the organic part occurs (Figure 1). We suggest that this broad signal (up to about 300 mT) can be related to the AcAc radical. Stabilization of the unpaired electron by delocalization (Scheme 3) leads to EPR line broadening.[28] As mentioned above, the formation of radical intermediates during decomposition of organic Mn(III)-containing salts is well-known;[24] therefore, our suggestion seems to be possible.

**Scheme 3. Resonance Structures of the AcAc Radical**

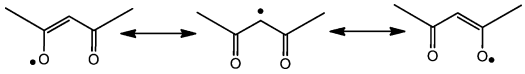

The EPR experiments can help to link the temperature behavior of the pure catalyst precursor in an oxygen atmosphere with that in porous media containing heavy oil. We compared temperature dependencies of EPR spectra for $Mn(AcAc)_3$ and $Mn–Al_2O_3–$oil systems. In the latter case, the signal attributed to the AcAc radical was not observed. The analysis of transformation of EPR spectra with temperature allowed for detachment of the Lorentzian component with a $g$ factor of 2.01 that was detectable in all of the studied samples, irrespective of the presence of the $Al_2O_3$ template and oil. Consequently, we ascribe the obtained Lorentzian contribution specifically to Mn(II)-containing compounds.

We focus our further analysis on temperature variation of the line width of this component and its integrated intensity. The EPR line width contains information about interaction of spins with the chemical environment, whereas integrated intensity is proportional to the number of corresponding resonant spins in the sample.

As shown in Figure 6A (blue plots), the concentration of the Mn(II) ions increased significantly at 250 °C for pure $Mn(AcAc)_3$ as a result of its fast decomposition to $Mn(AcAc)_2$ (see Scheme 2). A further decline of the integral intensity of the EPR signal at temperatures above 270 °C is related to oxidation of Mn(II) ions to Mn(III). In the case of the catalyst dispersed in oil (red plots in Figure 6A), the maximum concentration of Mn(II) ions is reached at a lower temperature. We explain this by the presence of plenty organic matter, which can effectively converse Mn(III) ions to Mn(II), even at ambient temperature.

Figure 6B (blue plots) shows that the line width of the EPR signal related to Mn(II) ions decreases significantly at 250 °C for pure precatalyst. The properties of the paramagnetic centers in materials are defined by their local magnetic and electrical environment. Therefore, the EPR spectra and EPR parameters are sensitive to the different types of phase transitions.[29−33] In the case of ions concentrated in crystal, the EPR line width contains information about dipole−dipole, crystal field, and exchange interactions between the paramagnetic centers and neighboring nuclei, atoms, and electrons. Thus, the sharp decrease of the line width observed in the region of organic part decomposition (according to XRPD and TGA data) can be associated with the transition from the organic to the inorganic crystal phase.

Even though the temperatures of the phase transition as observed in Figure 6 coincide for pure $Mn(AcAc)_3$ powder and its mixture with oil and $Al_2O_3$, one can notice substantial differences in the temperature dependence of the integral intensity below 250 °C. Together with the fact that the signal associated with AcAc was detected only in pure $Mn(AcAc)_3$ powder, this could indicate that different intermediate paramagnetic compounds form during the phase transition in these two samples. With this being said, we can use our conclusions for the analysis of the effect of the catalyst on heavy oil oxidation in porous media. We propose the following catalytic cycle based on our current investigation (Figure 7).

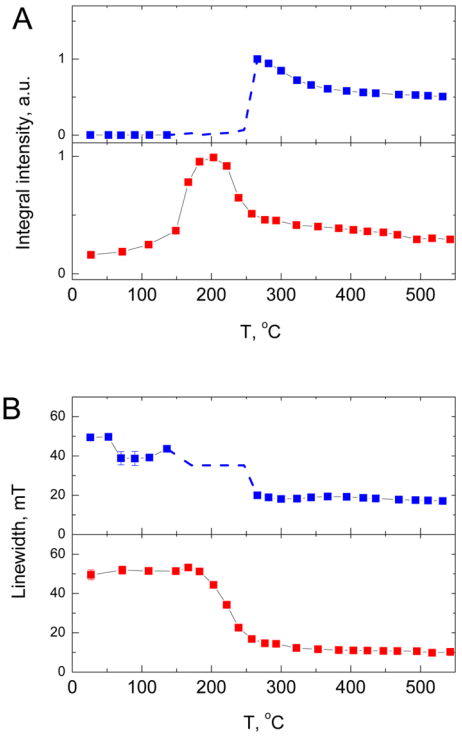


**Figure 6.** Temperature dependencies of the (A) normalized relative intensity and (B) width of the EPR line (for details, see the discussion in the text) detected during decomposition for pure $Mn(AcAc)_3$ powder (upper curves, blue plots) and $Mn–Al_2O_3–$oil (lower curves, red plots). The data shown by a dashed line correspond to the region where the signal attributed to the AcAc radical is observed (cf. Figure 5) and were evaluated by a multivariate curve resolution approach by assuming a constant line width.

To quantify kinetic parameters, such as effective activation energy ($E_a$) and Arrhenius constant ($A$), for both catalytic and non-catalytic oxidation processes, we applied an isoconversional (model-free) approach. The rate of many thermally stimulated processes proceeding in the condensed phase can be described

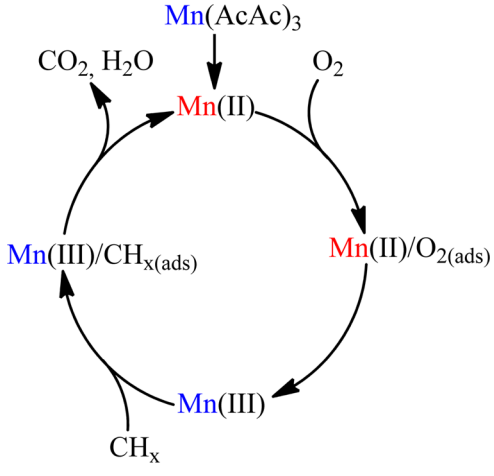


**Figure 7.** Proposed catalytic cycle.



DOI: 10.1021/acs.energyfuels.6b01234
Energy Fuels 2016, 30, 7731−7737

as a function of the absolute temperature ($T$) and extent of conversion ($\alpha$).

$$\frac{d\alpha}{dt} = k(T)f(\alpha) \quad (1)$$

The isoconversional approach originates from the isoconversional principle that states that the process rate at a constant extent of conversion is only a function of the temperature. This allows us to eliminate the reaction model $f(\alpha)$ from kinetic computations (eq 2).

$$\left[\frac{\partial \ln\left(\frac{d\alpha}{dt}\right)}{\partial T^{-1}}\right]_{\alpha} = \left[\frac{\partial \ln k(T)}{\partial T^{-1}}\right]_{\alpha} \quad (2)$$

The rate constant $k(T)$ is assumed to obey the Arrhenius law (eq 3).

$$k(T) = Ae^{-E_a/RT} \quad (3)$$

In this study, two integral methods, namely, Kissinger–Akahira–Sunose (KAS) and Ozawa–Flynn–Wall (OFW), were applied to DSC data. These methods are standard benchmarks, allowing for the calculation of kinetic parameters without any reaction model estimation.[20,34−36]

Usually two consecutive chemical processes occurred during heavy oil oxidation, namely, low-temperature oxidation (LTO) and high-temperature oxidation (HTO).[35] During LTO, hydrocarbons are broken and oxidized to give partially oxygenated hydrocarbons.[37] The HTO process is usually described as coke oxidation, producing carbon oxides and water.[38] Figure 8A shows a DSC curve for the non-catalytic heavy oil oxidation process, which is quite typical. In the case of catalytic oxidation, the third middle-temperature oxidation (MTO) peak appears that we supposedly relate to the catalytic oxidation process (Figure 8B). EPR and XPRD data prove this suggestion (Figures 2 and 3), showing the formation of a significant amount of Mn(III) at a temperature higher than 300 °C. Analyzed DSC intervals, the heat of reactions for each run, and examples of peak separation for DSC curves are presented in the Supporting Information.

Table 2 gives percentages of peak areas that are proportional to the heat of reactions ($\Delta H$; see the Supporting Information),

**Table 2. Percentages of Peak Areas after Peak Fitting for Catalytic and Non-catalytic Processes**

| | non-catalytic | | catalytic | | |
|---|---|---|---|---|---|
| heating rate (°C/min) | LTO | HTO | LTO | MTO | HTO |
| 5 | 38.6 | 61.4 | 47.5 | 36.2 | 16.3 |
| 10 | 37.9 | 62.1 | 49.6 | 31.1 | 19.3 |
| 15 | 38.3 | 61.7 | 51.6 | 25.0 | 23.4 |
| 20 | 39.6 | 60.4 | 53.4 | 21.2 | 25.4 |

and in the case of the non-catalytic process, the ratio of $\Delta H_{(LTO)}/\Delta H_{(HTO)}$ is almost independent of the heating rate.

Table 3 contains effective activation energies and Arrhenius constants for both non-catalytic and catalytic processes. All applied methods give similar results and show that manganese oxide nanoparticles formed *in situ* from $Mn(AcAc)_3$ significantly influence heavy crude oil combustion. In the case of HTO, a significant share of it starts to proceed at a lower temperature with the lower activation energy. Calculated effective activation energies in the case of the catalytic version of the experiment are much lower than that for the non-catalytic process. Differences between averaged effective $E_a$ for non-catalytic (n-c) and catalytic (c) versions are 11 kJ/mol ($LTO_{n\text{-}c} - LTO_c$), and 22 kJ/mol ($HTO_{n\text{-}c} - MTO_c$). This provides evidence about the effectivity of a catalyst for the oxidation process.

It should be noted that model-free methods bear possible errors resulting from the assumption of reaction rate dependency upon the temperature and conversion degree only. In OFW and KAS methods, activation energy is accepted as a constant all over the reaction. Nevertheless, the KAS method is more accurate as a result of its better approximation of the temperature integral.[39]

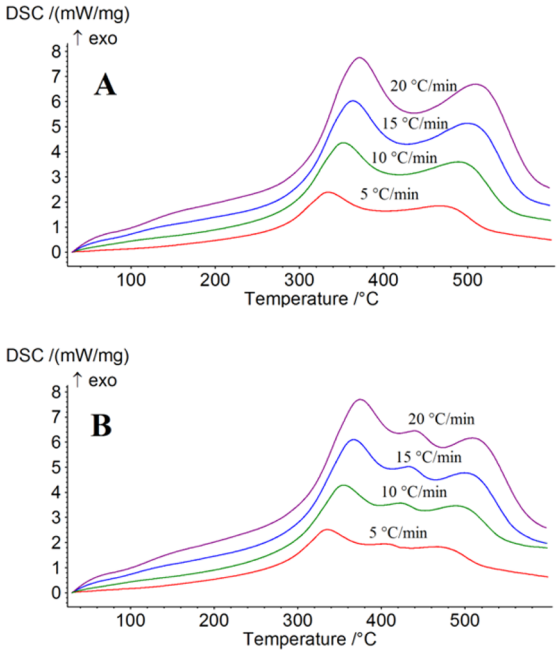


**Figure 8.** DSC curves of (A) non-catalytic and (B) catalytic heavy oil oxidation processes.

## 4. CONCLUSION

In summary, we investigated heavy oil oxidation in porous media in the presence of catalytically active manganese species formed *in situ* from $Mn(AcAc)_3$ as a precatalyst. Reaction kinetics in the heavy oil oxidation indicated that the presence of the manganese ions decreases the activation energy of the oxidation process, especially in the high-temperature region, compared to the non-catalytic process. To study the formation of active manganese species from precatalyst in details, we used an approach combining XRPD, thermal analysis, non-isothermal kinetic methods, and EPR. It is worth noting that a full understanding of the mechanism of heavy oil catalytic oxidation in porous media is an extremely difficult issue as a result of the complex nature of the phenomena, including heat and mass transfer, phase transitions, and hundreds of homo- and heterogeneous chemical reactions. Nevertheless, we believe that the suggested approach helps to clarify some aspects related to hydrocarbon catalytic oxidation.



DOI: 10.1021/acs.energyfuels.6b01234
Energy Fuels 2016, 30, 7731−7737

Table 3. Effective Activation Energy (kJ/mol) of Catalytic and Non-catalytic Processes

| | | $E_a$ (kJ/mol) [log $A$ ($s^{-1}$)] | | |
|---|---|---|---|---|
| sample | method | LTO | MTO | HTO |
| non-catalytic | KAS | 117.3 ± 2.4 [7.55] | | 158.8 ± 2.9 [8.45] |
| | OFW | 117.6 ± 0.6 [7.57] | | 150.6 ± 2.8 [7.85] |
| catalytic | KAS | 106.2 ± 3.8 [6.46] | 129.9 ± 6.5 [7.31] | 153.9 ± 1.6 [8.20] |
| | OFW | 106.9 ± 2.8 [6.47] | 136.4 ± 10.6 [7.83] | 155.6 ± 3.3 [8.30] |

## ■ ASSOCIATED CONTENT

### Supporting Information

The Supporting Information is available free of charge on the ACS Publications website at DOI: 10.1021/acs.energyfuels.6b01234.

Details on the control of the $Mn(AcAc)_3$ purity, peak-fitting procedure results, DSC reaction intervals, heat of reactions, and EDX analysis results (PDF)

## ■ AUTHOR INFORMATION


### Corresponding Author

*Telephone: +79172758404. E-mail: and_galuhin@mail.ru.


### Notes

The authors declare no competing financial interest.

## ■ ACKNOWLEDGMENTS

The reported study was funded by the Russian Foundation for Basic Research (RFBR), according to the Research Project 16-33-60085 mol_a_dk. This work was performed according to the Russian Government Program of Competitive Growth of Kazan Federal University. Sergei Orlinskii acknowledges the support of the subsidy allocated to Kazan Federal University in its project part. The authors thank Dr. Yuri Osin (Interdisciplinary Center for Analytical Microscopy, Kazan Federal University) for SEM measurements.

## ■ NOMENCLATURE

XRPD = X-ray powder diffraction
EPR = electron paramagnetic resonance
TEOR = thermally enhanced oil recovery
ISC = *in situ* combustion
SARA = saturate, aromatic, resin, and asphaltene
API = American Petroleum Institute
AcAc = acetylacetonate
DSC = differential scanning calorimetry
TGA = thermogravimetric analysis
SEM = scanning electron microscopy
ALS = alternating least squares
EDX = energy-dispersive X-ray spectroscopy
HF = hyperfine
KAS = Kissinger–Akahira–Sunose
OFW = Ozawa–Flynn–Wall
LTO = low-temperature oxidation
MTO = middle-temperature oxidation
HTO = high-temperature oxidation

## ■ REFERENCES


(1) Meyer, R. F.; Attanasi, E. D.; Freeman, P. A. *Heavy Oil and Natural Bitumen Resources in Geological Basins of the World*; United States Geological Survey (USGS): Reston, VA, 2007; USGS Open-File Report 2007-1084, pp 17–18.

(2) Giacchetta, G.; Leporini, M.; Marchetti, B. *Appl. Energy* **2015**, *142*, 1–9.

(3) Shah, A.; Fishwick, R.; Wood, J.; Leeke, G.; Rigby, S.; Greaves, M. *Energy Environ. Sci.* **2010**, *3*, 700–714.

(4) Akkutlu, I. Y.; Yortsos, Y. C. *Combust. Flame* **2003**, *134*, 229–247.

(5) Baud, G.; Salvador, S.; Debenest, G.; Thovert, J.-F. *Energy Fuels* **2015**, *29*, 6780–6792.

(6) Abuhesa, M. B.; Hughes, R. *Energy Fuels* **2009**, *23*, 186–192.

(7) Piumetti, M.; Fino, D.; Russo, N. *Appl. Catal., B* **2015**, *163*, 277–287.

(8) Santos, V.; Pereira, M.; Orfao, J.; Figueiredo, J. *Appl. Catal., B* **2010**, *99*, 353–363.

(9) Saqer, S. M.; Kondarides, D. I.; Verykios, X. E. *Appl. Catal., B* **2011**, *103*, 275–286.

(10) Garcia, T.; Sellick, D.; Varela, F.; Vázquez, I.; Dejoz, A.; Agouram, S.; Taylor, S. H.; Solsona, B. *Appl. Catal., A* **2013**, *450*, 169–177.

(11) Kuwahara, Y.; Yoshimura, Y.; Yamashita, H. *Catal. Sci. Technol.* **2016**, *6*, 442–448.

(12) Huang, G.; Luo, J.; Deng, C. C.; Guo, Y. A.; Zhao, S. K.; Zhou, H.; Wei, S. *Appl. Catal., A* **2008**, *338*, 83–86.

(13) Ferrandon, M.; Carnö, J.; Järås, S. G.; Björnbom, E. *Appl. Catal., A* **1999**, *180*, 141–151.

(14) Wang, F.; Dai, H.; Deng, J.; Bai, G.; Ji, K.; Liu, Y. *Environ. Sci. Technol.* **2012**, *46*, 4034–4041.

(15) Najjar, H.; Lamonier, J.-F.; Mentré, O.; Giraudon, J.-M.; Batis, H. *Catal. Sci. Technol.* **2013**, *3*, 1002–1016.

(16) Galukhin, A.; Erokhin, A.; Osin, Y.; Nurgaliev, D. *Energy Fuels* **2015**, *29*, 4768–4773.

(17) Varfolomeev, M.; Nagrimanov, R.; Galukhin, A.; Vakhin, A.; Solomonov, B.; Nurgaliev, D.; Kok, M. J. *J. Therm. Anal. Calorim.* **2015**, *122*, 1375–1384.

(18) Bhattacharjee, M.; Chaudhuri, M.; Khathing, D. *J. Chem. Soc., Dalton Trans.* **1982**, 669–670.

(19) Arhangel'skii, I.; Dunaev, A.; Makarenko, I.; Tikhonov, N.; Tarasov, A. *Non-isothermal Kinetic Methods: Workbook and Laboratory Manual*; Max Planck Research Library for the History and Development of Knowledge: Berlin, Germany, 2013.

(20) Vyazovkin, S.; Burnham, A. K.; Criado, J. M.; Pérez-Maqueda, L. a.; Popescu, C.; Sbirrazzuoli, N. *Thermochim. Acta* **2011**, *520*, 1–19.

(21) Biktagirov, T.; Gafurov, M.; Volodin, M.; Mamin, G.; Rodionov, A.; Izotov, V.; Vakhin, A.; Isakov, D.; Orlinskii, S. *Energy Fuels* **2014**, *28*, 6683–6687.

(22) Efron, B. *The Jackknife, the Bootstrap and Other Resampling Plans*; Society for Industrial and Applied Mathematics (SIAM): Philadelphia, PA, 1982.

(23) Jaumot, J.; Gargallo, R.; De Juan, A.; Tauler, R. *Chemom. Intell. Lab. Syst.* **2005**, *76*, 101–110.

(24) Mondal, M.; Bora, U. *RSC Adv.* **2013**, *3*, 18716–18754.

(25) Altshuler, S. A.; Kozyrev, B. M. *Electron Paramagnetic Resonance in Compounds of Transition Elements*, 2nd ed.; Halsted-Wiley: New York, 1974.

(26) Srinivasan, G.; Seehra, M. *Phys. Rev. B: Condens. Matter Mater. Phys.* **1983**, *28*, 1–7.

(27) Mukherjee, S.; Pal, A.; Bhattacharya, S.; Raittila, J. *Phys. Rev. B: Condens. Matter Mater. Phys.* **2006**, *74*, 104413.

(28) Eaton, G.; Eaton, S.; Salikhov, K. *Foundations of Modern EPR*; World Scientific: Singapore, 1998; pp 70–72.

(29) Jain, V.; Lehmann, G. *Phys. Status Solidi B* **1990**, *159*, 495–544.




DOI: 10.1021/acs.energyfuels.6b01234
*Energy Fuels* 2016, 30, 7731–7737

(30) Šimėnas, M.; Ciupa, A.; Mączka, M.; Pöppl, A.; Banys, J. *J. Phys. Chem. C* **2015**, *119*, 24522−24528.
(31) Gafurov, M.; Aminov, L.; Kurkin, I.; Izotov, V. *Supercond. Sci. Technol.* **2005**, *18*, 352−355.
(32) Gafurov, M.; Kurkin, I.; Kurzin, S. *Supercond. Sci. Technol.* **2005**, *18*, 1183−1189.
(33) Stößer, R.; Herrmann, W. *Molecules* **2013**, *18*, 6679−6722.
(34) Chen, B.; Castanier, L.; Kovscek, A. *Energy Fuels* **2014**, *28*, 868−876.
(35) Gundogar, A. S.; Kok, M. V. *Fuel* **2014**, *123*, 59−65.
(36) Kok, M.; Gundogar, A. *Fuel Process. Technol.* **2013**, *116*, 110−115.
(37) Sarathi, P. *In-Situ Combustion Handbook: Principles and Practices*; National Technology Information Service: Bartlesville, OK, 1999; pp 42−43.
(38) Khansari, Z.; Gates, I. D.; Mahinpey, N. *Fuel* **2014**, *115*, 534−538.
(39) Burnham, A.; Dinh, L. *J. Therm. Anal. Calorim.* **2007**, *89*, 479−490.



DOI: 10.1021/acs.energyfuels.6b01234
*Energy Fuels* 2016, 30, 7731−7737